Materials Characterization 203 (2023) 113118

Contents lists available at ScienceDirect

Materials Characterization

journal homepage: www.elsevier.com/locate/matchar

High-cycle fatigue failure behavior of nickel-based single crystal alloys with different deviation angles in a high-temperature environment

Zhuangzhuang Mao [a], Yingbin Zhu [a], Yao Zhao [a], Huimin Xie [b], Yanhong Yang [c], Yizhou Zhou [c], Xianfu Huang [d,*], Zhanwei Liu [a,*]

[a] School of Aerospace Engineering, Beijing Institute of Technology, Beijing 100081, China
[b] AML, Department of Engineering Mechanics, Tsinghua University, Beijing 100084, China
[c] Institute of Metal Research, Chinese Academy of Sciences, Shenyang 110016, China
[d] Institute of Mechanics, Chinese Academy of Sciences, Beijing 100190, China

ARTICLE INFO

Keywords:
Nickel-based single crystal
Different deviation angles
High cycle fatigue failure mechanism

ABSTRACT

The high-cycle fatigue failure behavior of nickel-based single crystal alloys with different deviation angles (deviated [001] orientations of 0°, 10°, and 20°) was assessed in this work. At 980 °C/600 MPa, the fatigue life decreases with increasing deviation angle from the [001] orientation.The dislocation motion is mainly Orowan deformation mechanism, and the fatigue mode is crystallographic fracture. At 980 °C/640 MPa, the fatigue life is the longest when the deviation angle is 0°, and it is the shortest when the deviation angle is 10°. The fatigue failure mode is the crystallographic fracture when the deviation angle is 0° and 20°, and it is the non-crystallographic fracture when the deviation angle is 10°. The dislocation motion is mainly a single dislocation or paired dislocation shearing γ' phase deformation mechanism.

1. Introduction

Aeroengine turbine blades are the key components that directly use high-temperature and high-speed gas as power. During the service period, the blade not only has to bear the load caused by the start and stop of the engine [1–4] but also bears the high-temperature creep damage caused by centrifugal force and the fatigue damage caused by stress and temperature changes. Its strength and reliability are directly related to the performance and service life of the engine [5]. Since the 1970s, with the development of directional solidification technology, nickel-based single-crystal alloys have been widely used in the manufacture of aero-engines and gas turbine blades due to their excellent comprehensive resistance to creep, fatigue, oxidation, and corrosion [6–9], which greatly increases the air inlet temperature at the front end of the turbine [10–14]. During the working process, the blade material is subjected to extreme service conditions, such as high temperature, high pressure, and high-speed rotation, for extended periods of time. Damage under high-temperature fatigue has become one of the main failure modes of such components, which usually break suddenly without obvious plastic deformation and often causes a major accident. In addition, because the nickel-based single crystal alloy has a preferred orientation of ⟨001⟩, the [001] orientation is selected as the main stress direction in the actual manufacturing process of turbine blades. However, the existence of orientation deviation in the process of directional solidification is difficult to avoid. On the other hand, one of the key technical measures to avoid resonance with the engine is to use nonaxial blades, that is, the blades are axially deviated from the [001] orientation by a certain angle. When the deviation angle exceeds a certain range, the mechanical properties of the alloy will change significantly.

At present, the influence of orientation deviation on the properties of nickel-based single-crystal alloys mainly focuses on the three crystal orientations [001], [011], and [111] [15–17]. The literature results indicated that the crystal orientation significantly affects the strain fatigue life of single-crystal alloys, among which the [001] orientation has the longest strain fatigue life and the [111] orientation has the shortest strain fatigue life [18,19]. Meanwhile, many scholars have only conducted research on deviations from the [001] orientation. Gu et al. [20] conducted a study on the creep properties of nickel-based high-temperature alloy specimens in the [001] direction. The results demonstrated a correlation between the size and position of the γ' phase, and indicated that the differences in microstructure and morphology had an impact on creep life. Furthermore, the creep life decreased with

* Corresponding authors.
E-mail addresses: huangxf@imech.ac.cn (X. Huang), liuzw@bit.edu.cn (Z. Liu).

https://doi.org/10.1016/j.matchar.2023.113118
Received 2 March 2023; Received in revised form 23 May 2023; Accepted 22 June 2023
Available online 25 June 2023
1044-5803/© 2023 Elsevier Inc. All rights reserved.

increasing stress. The work of Rac et al. [21] showed that at relatively low temperatures (e.g., 750 °C), within 20° of the [001] orientation, the degree of creep in the first stage was related to the small deviation angle close to the [001]–[011] symmetry boundary, while at high temperatures (e.g., 950 °C), the degree of creep deformation had little relationship with the deviation angle. Leverant et al. [22] researched the relationship between creep life and orientation deviation angle, and the results showed that with the increase in deviation angle from the [001] orientation, creep life decreased significantly. Zhang et al. [23] investigated the failure mechanisms and deformation behavior of nickelbased single crystal alloy DD6 with [001] orientation under fully reversed stress-controlled low cycle fatigue (LCF) loading at 980 °C. Through the scanning electron microscope (SEM) observations, it was shown that the failure characteristics under stress-controlled LCF loading were similar with those under strain-controlled loading. The LCF lifetimes under stress control were significantly shorter than the LCF lifetimes under strain control, and the culprit might be the detrimental effect of ratcheting strain on LCF lifetime. Fan et al. [24] researched the influence of the orientation deviation from [001] of a DD10 nickel-based single crystal alloy on the LCF life. The results showed that the low-cycle fatigue life decreased significantly with increasing orientation deviation. At the same time, the fatigue life was also related to the second orientation of the alloy; that was, under the same degree of deviation, the low-cycle fatigue life of alloys with orientations closed to [001]–[011] was higher than that of [001]–[111]. In summary, the influence of orientation deviation on the fatigue and creep properties of nickel-based single-crystal alloys cannot be ignored. At present, the influence of a small deviation angle on the mechanical properties of nickel-based single-crystal alloys mainly focuses on the tensile properties, creep life, and other aspects. However, little research has been done on the effect of small deviation angles on the high cycle fatigue properties of nickel-based single-crystal alloys. Therefore, it is necessary to research the effect of a small deviation angle on the high cycle fatigue life of nickel-based single-crystal alloys.

Accordingly, we conducted high-cycle fatigue experiments of nickel-based single-crystal alloys with small deviation angles, and the fatigue life at different deviation angles was obtained. The fracture morphologies of nickel-based single-crystal alloys with different stress amplitudes and different deviation angles before and after fatigue were compared, and their crack propagation behaviors were analyzed. At the same time, by comparing the microstructure changes of the two phases before and after the fatigue test, the microscopic failure mechanism was analyzed.

2. Materials and methods

Fig. 1 (a) shows the plate-like as-cast material of the nickel-based single crystal alloy. When cutting samples with different deviation angles, the angle only changes in the y-z plane, and the angle in the x direction remains unchanged. Fig. 1 (b) shows the typical dendritic structure morphology of the as-cast microstructure. The direction of the white arrow in Fig. 1 (b) is the direction of primary dendrite growth, which is the <001> orientation of the nickel-based single crystal alloy. Fig. 1 (d) is a schematic diagram of cutting blocks with deviation <001> orientations of 0°, 10°, and 20° according to the primary dendrite growth direction. The as-cast bulk samples are heat treated as follows: 1300 °C + 2 h air cooling; 1080 °C + 4 h air cooling; 1120 °C + 4 h air cooling; 900 °C + 4 h air cooling. The typical microstructure after heat treatment is shown in Fig. 1 (c). Fig. 1 (c) shows that the nickel-based single crystal is mainly composed of two phases, namely, the matrix γ phase and the γ' phase. Among them, the γ' phase is embedded in the matrix γ phase and is the main strengthening phase. The size of the γ' phase is between 300 and 500 nm, and the volume fraction accounts for approximately 70%.

Fig. 2 (a) is a schematic diagram of the specimen. The overall length of the specimen is 55 mm, the length of the working section is 12 mm, the width is 4 mm, and the thickness is 1.5 mm. Fig. 2 (b) shows the real sample and three main crystal orientations, and Fig. 2(c) is a schematic diagram of possible slip planes.

The high-cycle fatigue experiments were completed on a hydraulic servo testing machine, as shown in Fig. 3. The deviation angles of the specimens were 0°, 10°, and 20°. The experimental conditions were as follows: the temperature was $T = 980$ °C, stress ratio was $R = 0.1$, stress amplitudes were 600 MPa and 640 MPa, the tension-tension cyclic loading method was adopted, the loading waveform was a sine wave, and the loading frequency was f = 40 Hz.

To ensure that the surface conditions of the specimens were consistent, the surfaces of the specimens were mechanically polished before the experiment. Surface roughness has a significant effect on the fatigue properties of nickel-based single crystal alloys. In general, the greater the surface roughness, the shorter the fatigue life, but when the surface roughness is small to a certain extent, it has no effect on the fatigue life [25–27]. Therefore, it is necessary to perform surface mechanical polishing on the specimen. This work involved polishing the specimens

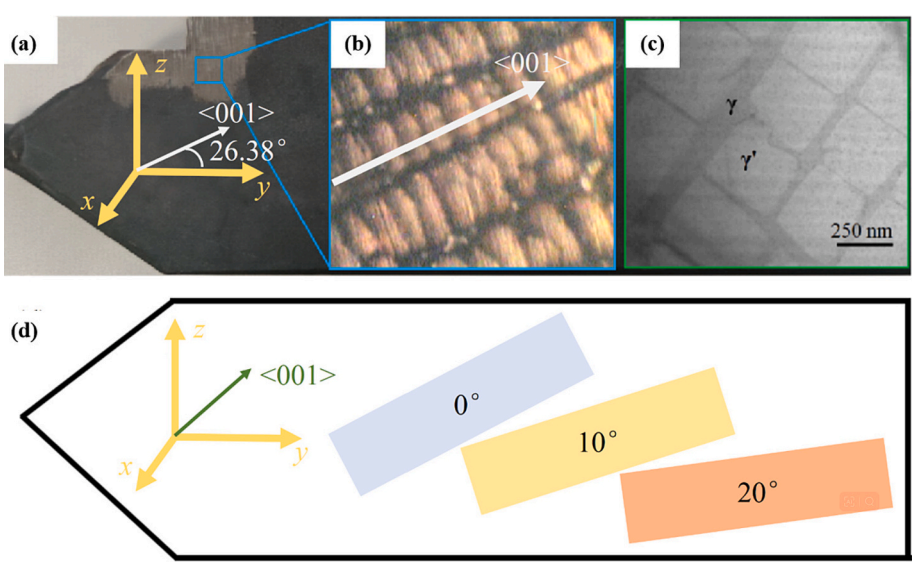

Fig. 1. (a) Nickel-based single-crystal alloy plate material, (b) as-cast microstructure, (c) microstructure after heat treatment, (d) schematic diagram of cutting block specimens with different deviation angles.

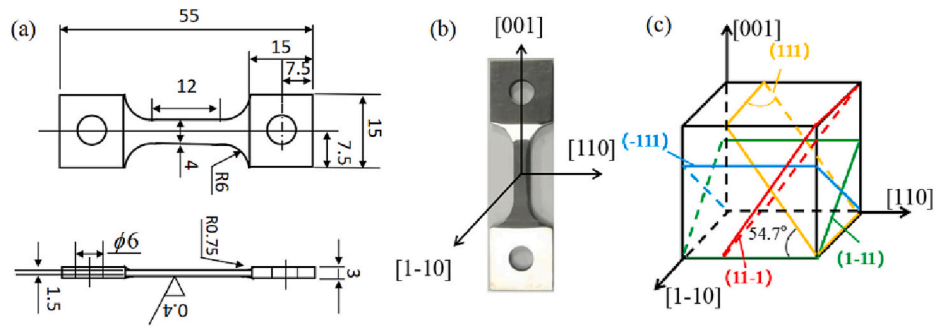

Fig. 2. (a) Schematic diagram of tensile specimen, (b) real specimen, (c) schematic diagram of slip surface.

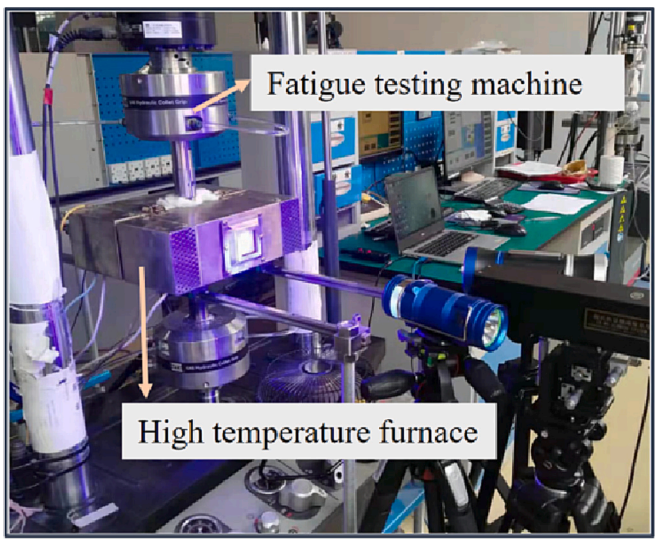

Fig. 3. Equipment for high-cycle fatigue experiment.

using different grades of sandpaper, ranging from 400 to 7000 grit, until the specimen surface became smooth and free from scratches. The specimens were then immersed in alcohol for 5 min and subjected to ultrasonic cleaning to remove impurities and particles adsorbed on the specimen surface during the grinding process. Subsequently, a diamond polishing agent with a particle size of 1 μm was used for deep-level polishing to remove minor scratches on the specimen surface. During this process, the specimen surface was repeatedly observed under an optical microscope until it became smooth. Afterwards, the samples were immersed in alcohol and cleaned in an ultrasonic cleaning machine for 5 min to remove any small particles adhering to the specimen surface.

After the experiment was completed, the fracture morphologies of the specimens with different deviation angles were analyzed by SEM (The SEM model is quanta 450 fegon). Transmission electron microscopy (TEM, The TEM model is FEI Tecnai G2 F20) was used to analyze the microstructure before and after fatigue. The transmission samples are fabricated by the focused ion beam (FIB), and the TEM image of sample sampling is shown in Fig. 4. Fig. 4 (a) shows the sample cutting position, and Fig. 4 (a) shows the cutting sample. The fatigue source is the location where crack initiation occurs, and it contains valuable information about crack initiation and propagation. In the analysis of fatigue fracture in nickel-based single crystal alloys, it plays a crucial role. Meanwhile, to ensure that all samples are in the same state and avoid the influence of necking near the fracture, samples are taken 1 mm below the fatigue source.

3. Experimental results and discussion

Fig. 5 shows the fatigue life of the specimens under different stress amplitudes and different deviation angles, and the fatigue life decreases with increasing stress amplitude. At 600 MPa/980 °C, the fatigue life decreases gradually with increasing deviation angle. When the deviation angle is 0°, the fatigue life is the longest, which is 1.678×10^6 cycles. When the deviation angle is 10°, the fatigue life is 3.83×10^5 cycles. When the deviation angle is 20°, the fatigue life is the shortest, which is 2.81×10^5 cycles. At 640 MPa/980 °C, the fatigue life is 7.82×10^5 cycles when the deviation angle is 0°, the fatigue life is 2.16×10^5 cycles when the deviation angle is 10°, and the fatigue life is the fatigue life is 2.53×10^5 cycles when the deviation angle is 20°.

Two experiments are conducted under the same conditions, and the fatigue life of each experiment is shown in Table 1. The green dots in Fig. 5 correspond to the fatigue life of each experiment. According to their distribution, at 0 °C, when the deviation angle is 0°, the dispersion degree of fatigue life is relatively large, and when the deviation angles are 10° and 20°, the dispersion degree of fatigue life is small, both scattered near the average value. Under the same temperature and

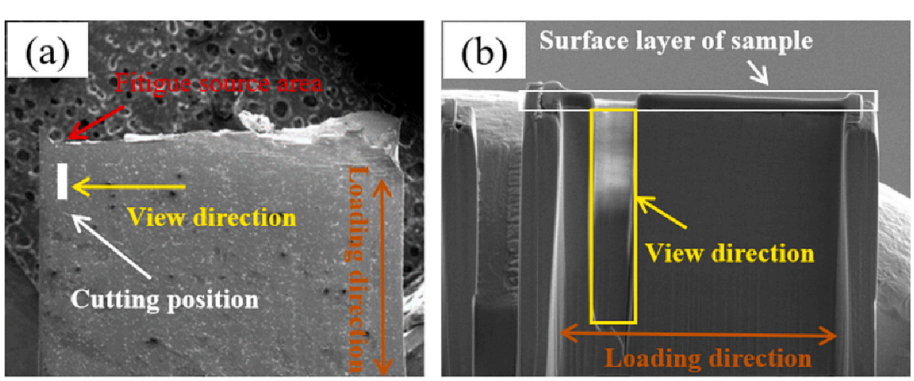

Fig. 4. TEM image of sample sampling, (a) sample cutting position, (b) cutting sample.

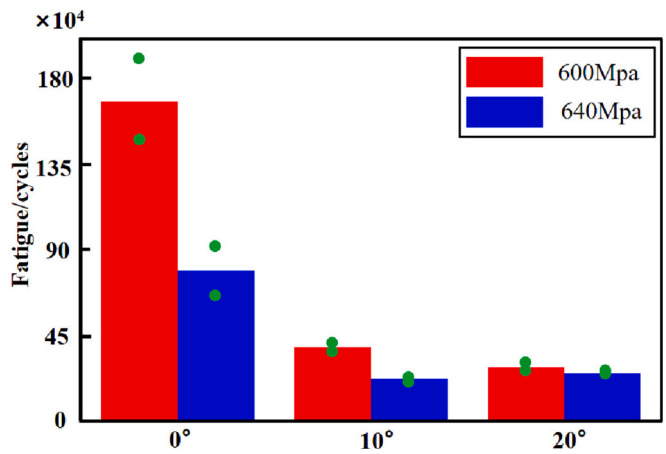

Fig. 5. Fatigue life under different stress amplitudes and different deviation angles.

Table 1
Fatigue life of each experiment.

Deviation angles / stress / temperature	Fatigue life (×104) / cycles		Average / cycles
0°/600 MPa/980 °C	189.4	146.2	167.8
10°/600 MPa/980 °C	41.2	35.4	38.3
20°/600 MPa/980 °C	30.2	26	28.1
0°/640 MPa/980 °C	64.5	91.9	78.2
10°/640 MPa/980 °C	22.4	20.8	21.6
20°/640 MPa/980 °C	26.3	24.3	25.3

stress, the fatigue life of samples with different deviation angles varies significantly. The fatigue life with the 0° deviation angle is 3.2–5.9 times that with the 10° and 20° deviation angle, indicating a certain degree of dispersion in the overall fatigue life.

3.1. Fatigue fracture behavior at 980 °C/600 MPa

The macroscopic morphology of the fatigue fracture of the nickel-based single-crystal alloy is shown in Fig. 6. Under a stress amplitude of 600 MPa, the high-cycle fatigue fractures of the samples with different deviation angles have typical fatigue fracture characteristics, which are composed of three parts: the fatigue source area, the crack growth area and the fast fracture area. The initiation sources of fatigue cracks are the large shrinkage cavities near the subsurface of the sample. During the fatigue process, the position of the shrinkage cavity is subjected to stress concentration, where microcracks nucleate, initiate and develop, and then evolve and expand to the interior and surface of the sample. Simultaneously, significant deformation has occurred in the shrinkage cavity of the fatigue source area, with radiation lines present at specific angles. This not only indicates that during the fatigue process, cracks initiate at the internal shrinkage cavities of the sample and propagate along specific slip planes {111}, but also suggests that the crack initiation mechanism follows a crystallographic crack initiation mode.

The green area in Fig. 6 is the fatigue source area. The fatigue source area is delicate and smooth, and the brightness is high. During the fatigue loading process, the microcracks are repeatedly squeezed along the loading direction throughout the entire life cycle to form flat, smooth, and even shiny sections. When the deviation angle is 0°, the existence of two fatigue source areas is observed, as shown in the green area in Fig. 6 (a). Shrinkage cavities close to the subsurface of the plate samples are subject to greater stress concentrations. During the fatigue process, fatigue source 1 is the main crack source, which is elliptical. In the fatigue process, it first entered the crack propagation zone, supplemented by internal fatigue source 2, and finally, the sample fractured under the combined action of the two fatigue cracks. When the deviation angle is 10°, the fatigue source area is circular with a diameter of 540 μm, and inclusions such as carbides are found, as shown in Fig. 6 (b). A stress concentration area is easily formed near the inclusions, leading to the initiation of microcracks. When deviated from 20°, the fatigue source area is arc-shaped with a diameter of approximately 600 μm. From the crack propagation in the fatigue source region, it is found that crystallographic cracks are initiated in samples with different deviation angles.

A relatively smooth and clean fan-shaped area that could be seen at the same time on the fatigue fracture is the crack extension area (as shown in the yellow fan-shaped area in Fig. 6), which indicates the presence of cleavage fracture features.

When the crack propagates until the remaining area of the material itself is not sufficient to withstand the applied load, it will form a fast fracture area as shown in the blue box in Fig. 6. There are no obvious dimples in this area, and there are continuous steps of different heights, which are caused by the simultaneous initiation of cracks along with different {111} plane slip systems during the fatigue process. The fatigue cracks zigzag and expand along different slip surfaces and continuously merge to form fatigue steps, and each step represents a certain cycle. The width of the fatigue step increases as the number of fatigue cycles increases, so the direction of crack propagation can be judged along the width direction of the step.

When deviated from 10°, the area size of the fatigue step is not uniform, which indicates that the plastic deformation is not uniform during the fatigue process, as shown in the blue area of Fig. 6 (b). When the deviation angle is 20°, the second orientation of the sample gradually approaches the [111] direction, resulting in the fracture area being divided into two parts. One part is a relatively smooth plane, and its fracture process proceeds along the (−111) slip plane, while the other part is formed by the simultaneous operation of different {111} plane slip systems to form fatigue steps, as shown in the blue area in Fig. 6 (c). At 980 °C/600 MPa, as shown in Fig. 6, numerous fatigue steps are observed in the fracture area of samples with different deviation angles, which is caused by the simultaneous initiation of cracks along different {111} plane slip systems during the fatigue process. This indicates that the fatigue mode of the nickel-based single crystal alloy at 980 °C/600 MPa is crystallographic fracture.

The fatigue life of alloys during high cycle fatigue is determined by the fatigue source area and the crack growth area. The larger the area occupied by the fatigue source area and the crack growth area is, the longer the crack propagation time, and therefore the longer the fatigue life. When deviating from 0°, the fatigue source area and the crack growth area are the largest, with a radius of approximately 1210 μm; when the deviation is 10°, the radius is approximately 1120 μm; and when the deviation is 20°, the radius is approximately 1050 μm. The fatigue life gradually decreases with increasing deflection angle during the fatigue process.

3.2. Fatigue fracture behavior at 980 °C/640 MPa

As the stress amplitude increases from 600 MPa to 640 MPa, the area occupied by the fatigue source area and the expansion area in the fracture decreases, while the area occupied by the fracture area increases. Under the combined action of stress concentration and local plastic deformation, the initiation area of fatigue cracks changes. Cracks are mainly initiated on the surface or subsurface, or in the shrinkage porosity inside the sample, the fracture has a larger flat slip plane, and the fatigue step in the fracture area is wider. Similar to the case at 980 °C/600 MPa, significant deformation has occurred in the shrinkage cavity of the fatigue source area, with radiation lines present at specific angles. This indicates that the crack initiation mechanism follows a crystallographic crack initiation mode.

When the deviation angle is 0°, larger fatigue striations are observed, as shown in Fig. 7 (a). The fatigue striations are arc-shaped and gradually increase, and the spacing between adjacent fatigue striations

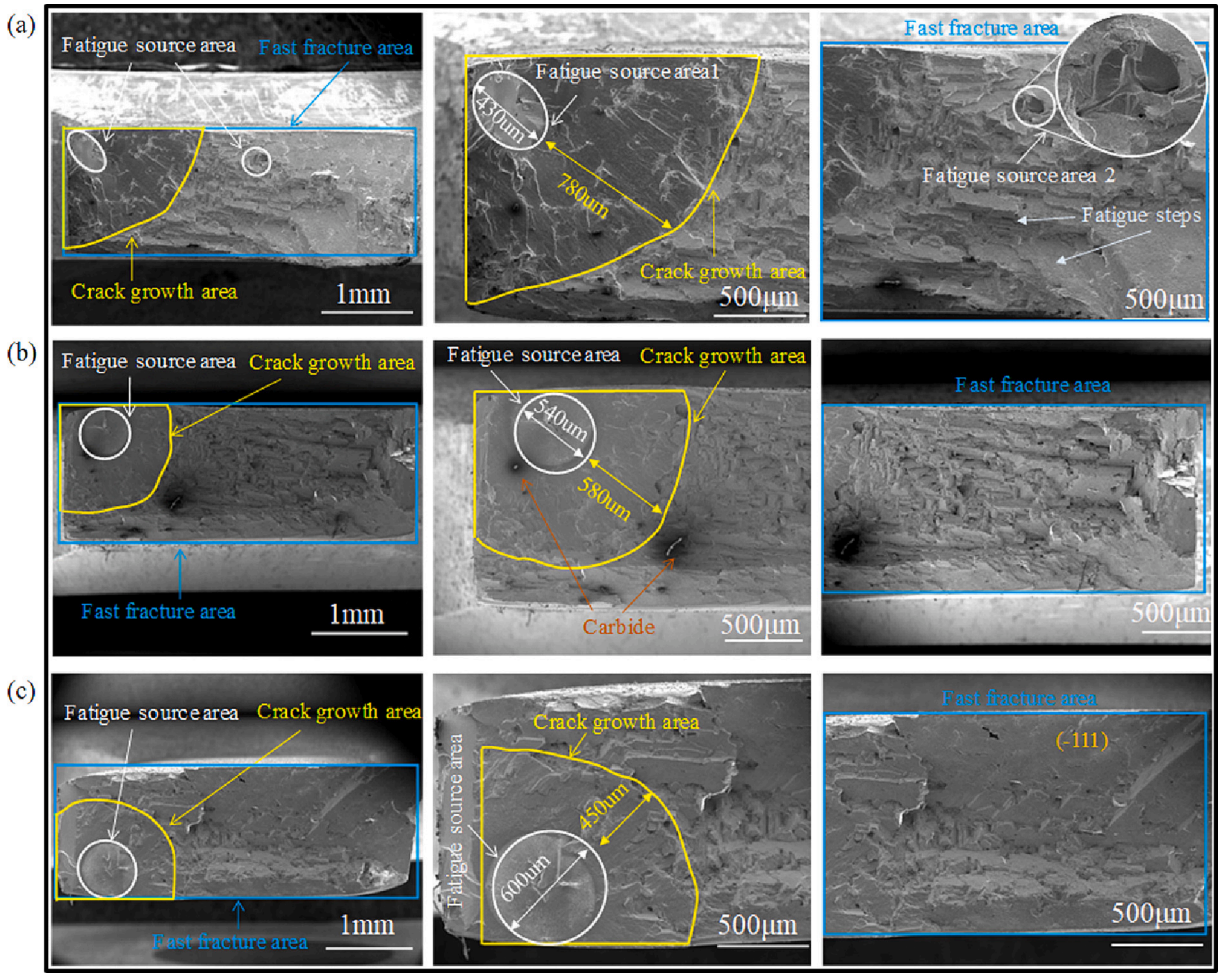

Fig. 6. Fatigue fracture morphologies of nickel-based single-crystal alloy samples with different deviation angles at 980 °C /600 MPa: (a) 0°, (b) 10°, (c) 20°.

increases. The growth rate of fatigue cracks is small at the initial stage of fatigue, so the spacing of fatigue fringes during fatigue is small. As the number of fatigue cycles increases, the opening displacement of the crack increases gradually, and the growth rate also increases gradually, which leads to an increase in the spacing of fatigue striations. The propagation direction of the crack is perpendicular to the fatigue striation, and there are multiple propagation directions to the crack, as shown by the black arrow in Fig. 7 (a). At the same time, during the crack propagation process, the precipitated carbides will change the direction of crack propagation, as shown by the yellow arrows in Fig. 7 (a). When the deviation angle is 0°, the initial fatigue crack mainly initiates and propagates along the (111) plane. The fracture area is a smooth inclined plane, which is identified as a (1−11) slip plane. Therefore, when the deviation angle is 0°, the fracture mode of the nickel-based single crystal alloy is crystallographic fracture.

Fig. 7 (b) shows that the fatigue crack originated at the shrinkage cavity inside the sample, there is an obvious fatigue source area, and the crack source area is relatively smooth. At this stage, the opening displacement of the microcrack is small, and the crack propagation is relatively slow. Due to the repeated opening and closing of the crack, the two sides of the fracture are squeezed and rubbed against each other, and the most delicate and smooth area is formed at the fracture. When the deviation angle is 10°, the crack propagation area of the sample becomes significantly smaller, which greatly affects the fatigue life of the sample. It can be seen from the fracture area that when the deviation angle is 10°, the nickel-based single crystal alloy is an amorphous fracture, as shown in the blue box in Fig. 7.

When the deviation angle is 20°, the fatigue source area starts from the subsurface shrinkage cavity of the sample. The fatigue cracks propagate along two crystallographic planes, namely, the slip planes (1–11) and (−111) intersect along the ⟨110⟩ direction to form a conjugate fracture plane, which indicates that the two slip planes start simultaneously during the fatigue failure process, as shown in Fig. 7 (c). This is due to the influence of the second orientation of the sample (closer to the [111] crystallographic orientation) on the propagation of fatigue cracks when the deviation angle is 20°. The crack growth rate increases with increasing cycle number, and the distance between adjacent fatigue striations on the (1–11) slip surface also increases. A fast fracture area is a smooth plane, indicating that the crack propagates along the (1–11) slip plane until it breaks. The crack propagates along different slip planes and forms a fatigue step composed of two approximately vertical cleavage planes. Each fatigue step corresponds to a certain number of cycles. In the initial stage of step formation, the crack propagation rate is slow, and the step width is small. As the cyclic loading progresses, the expansion rate increases, and the fatigue step width increases. When the deviation angle is 20°, it is a typical crystal fatigue failure mode.

3.3. Behavior of carbide precipitation at longitudinal fracture surface

Fig. 8 (a) shows the longitudinal section of the sample after the fatigue fracture under the SEM, and many bright silver precipitates are observed near the longitudinal fracture surface. To determine the composition of the precipitates, the energy dispersive X-ray spectrometer (EDS) point scanning is used to analyze the elemental composition in the precipitates, as shown in Fig. 8 (b). After point scanning, it is

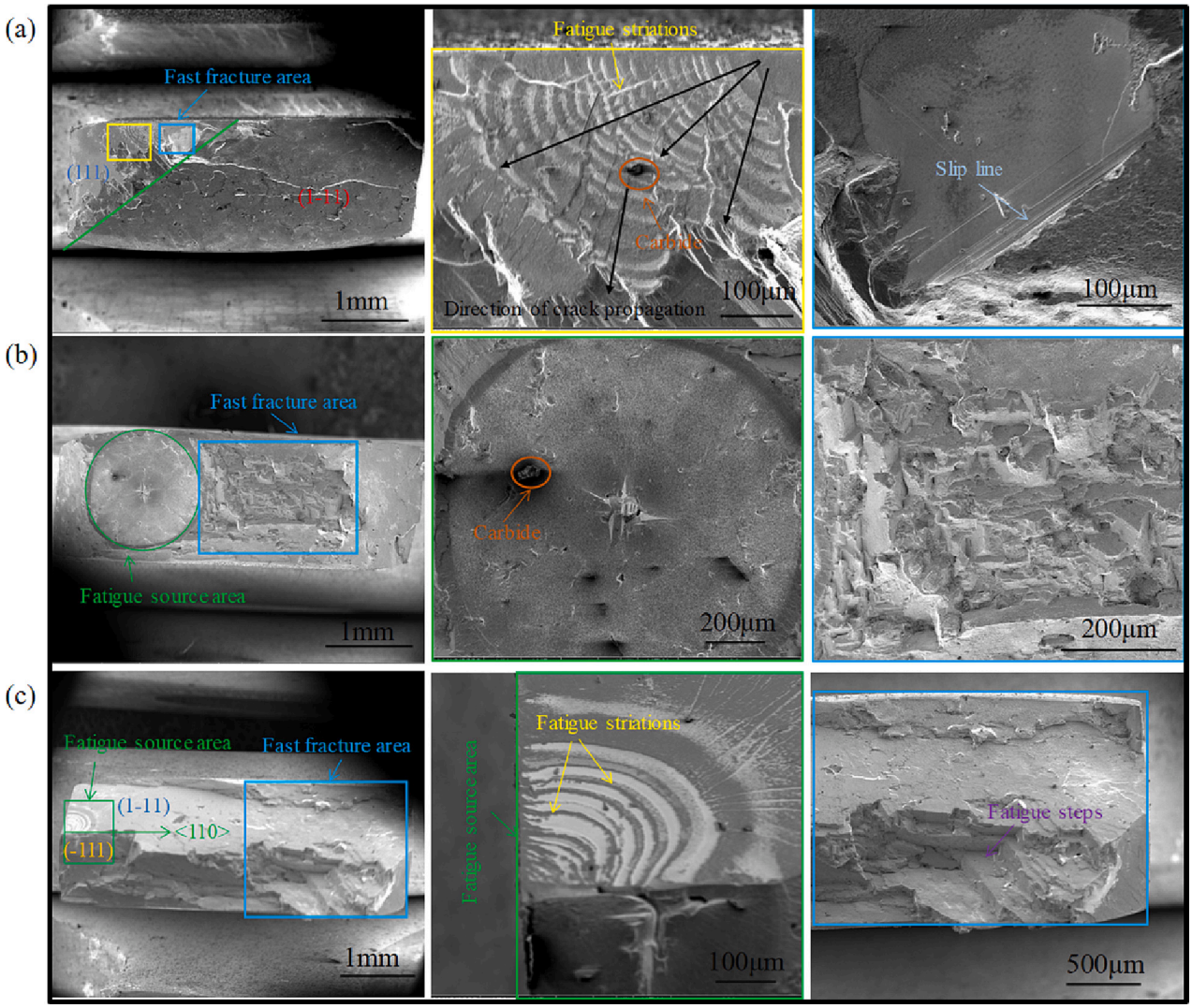

Fig. 7. Fatigue fracture morphologies of nickel-based single-crystal alloy samples with different deviation angles at 980 °C/640 MPa: (a) 0°, (b) 10°, (c) 20°.

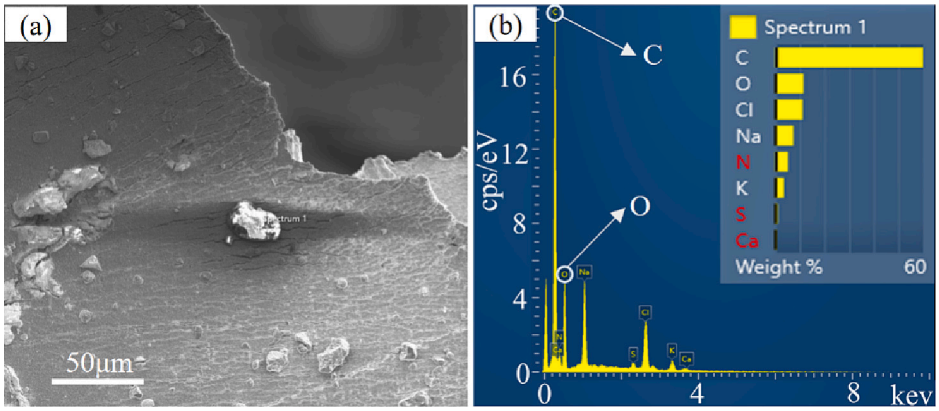

Fig. 8. (a) Longitudinal section of sample under SEM after fatigue fracture, (b) elemental composition in precipitates.

determined that the main elements in the bright silver precipitates are C and O, and the precipitates near the fracture after fatigue are mainly carbides.

During the high-cycle fatigue, single crystal alloys experience diffusion behavior of elements influenced by external loads and temperature. Due to the long fatigue cycles and elevated temperatures, carbon elements have sufficient time to diffuse, significantly increasing the probability of carbon elements bonding with each other, leading to element clustering. Moreover, high concentrations of carbon elements precipitate in the form of carbides. The longer the fatigue life, the higher the content of precipitated carbides. Samples with a deviation angle of 0° exhibit the longest fatigue life and the highest content of precipitated

carbides, as shown in Fig. 9 (a) and Fig. 9 (d). Through observation, it has been found that the precipitated carbides during the fatigue process is mainly concentrated at the fracture locations, specifically at the crack propagation paths. This is because the fracture locations experience higher stress concentration compared to other regions of the sample during the fatigue process, creating certain stress gradients that provide driving forces for element precipitation in high-temperature fatigue. In the early stages of fatigue, the precipitation of fine carbides within the crystal can have a strengthening effect and improve the mechanical properties of the alloy. However, as the carbides continue to aggregate and grow during the later stages of fatigue, larger carbide particles become detrimental inclusions. Under the influence of external loading during the fatigue process, these inclusions experience stress concentration, promoting crack initiation at these locations, as indicated by the yellow arrows in Fig. 9 (b) and Fig. 9 (e). This crack initiation behavior is caused by the accumulation and growth of carbides. Additionally, during the crack propagation process, encountering inclusions such as carbides can alter the crack propagation path, as shown by the green arrows in Fig. 9.

3.4. Evolution behavior of dislocation population at 980 °C/600 MPa

Fig. 10 shows the scanning transmission electron microscopy (STEM) images near the fatigue source of Ni-based single-crystal alloys with different deviation angles after fatigue fracture under a load of 980 °C/600 MPa. There are dislocation network structures with different deflection angles in the fatigue samples of the nickel base single crystal alloy because dislocations first appear in the γ phase with low yield strength. Then, as fatigue progresses, the dislocations move in the matrix γ phase under the action of the applied stress. When the dislocation encounters the relatively high intensity γ' phase, it will stop moving at the interface. The dislocations with a Burger vector of a/2 < 110> in the γ phase are captured by the γ/γ interface, and dislocations at multiple locations meet to form a network structure at the interface. The existence of the interfacial dislocation network prevents new dislocations in the γ phase from cutting into the γ' phase. When the deviation angle is 0°, a large number of dislocations are entangled in the γ phase, which hinders the movement of new dislocations and increases the resistance of other dislocations moving into the γ' phase. The dislocations climb into the γ' phase at the later stage of fatigue, as shown in Fig. 10 (c). There are dislocation loops in the γ phase at off-angles of 10° and 20° because the high strength of the γ' phase makes it difficult for the dislocation to cut the γ' phase and eventually bend and move around the γ' phase. Fig. 10 (d), Fig. 10 (h) and Fig. 10 (i) show that the morphology of the γ' phase after fatigue fracture changes from cubic to irregular shape. That is, the "dissolution" of the γ' phase occurs, and the direct result of the dissolution is the broadening of the γ-phase channel in the matrix. Even within the same sample, the dissolution process is not

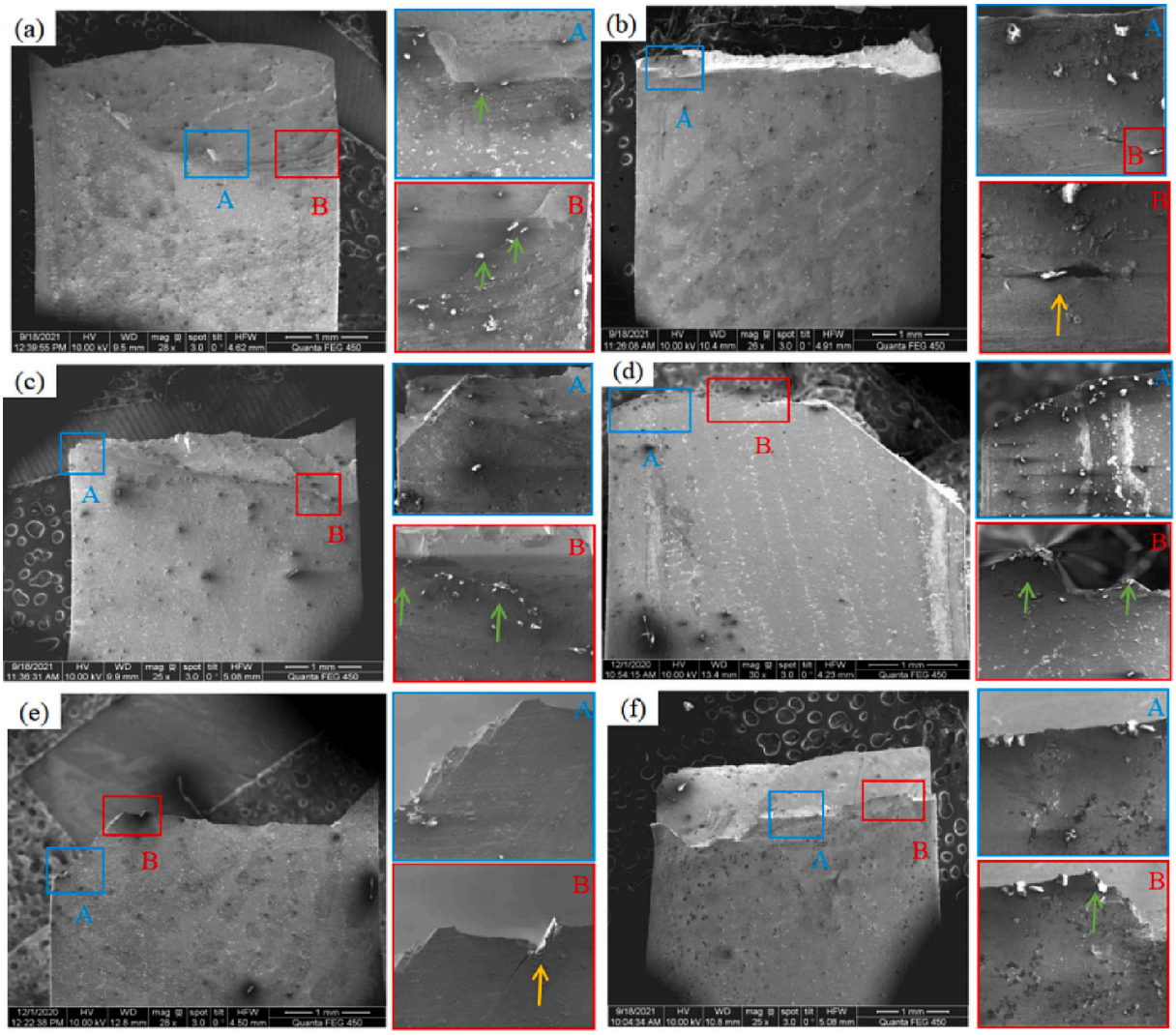

Fig. 9. Precipitated carbides near fracture surface under different stresses and deviation angles: (a) 600 MPa, 0°, (b) 600 MPa, 10°, (c) 600 MPa, 20°, (d) 640 MPa, 0°, (e) 640 MPa, 10°, (f) 600 MPa, 20°.

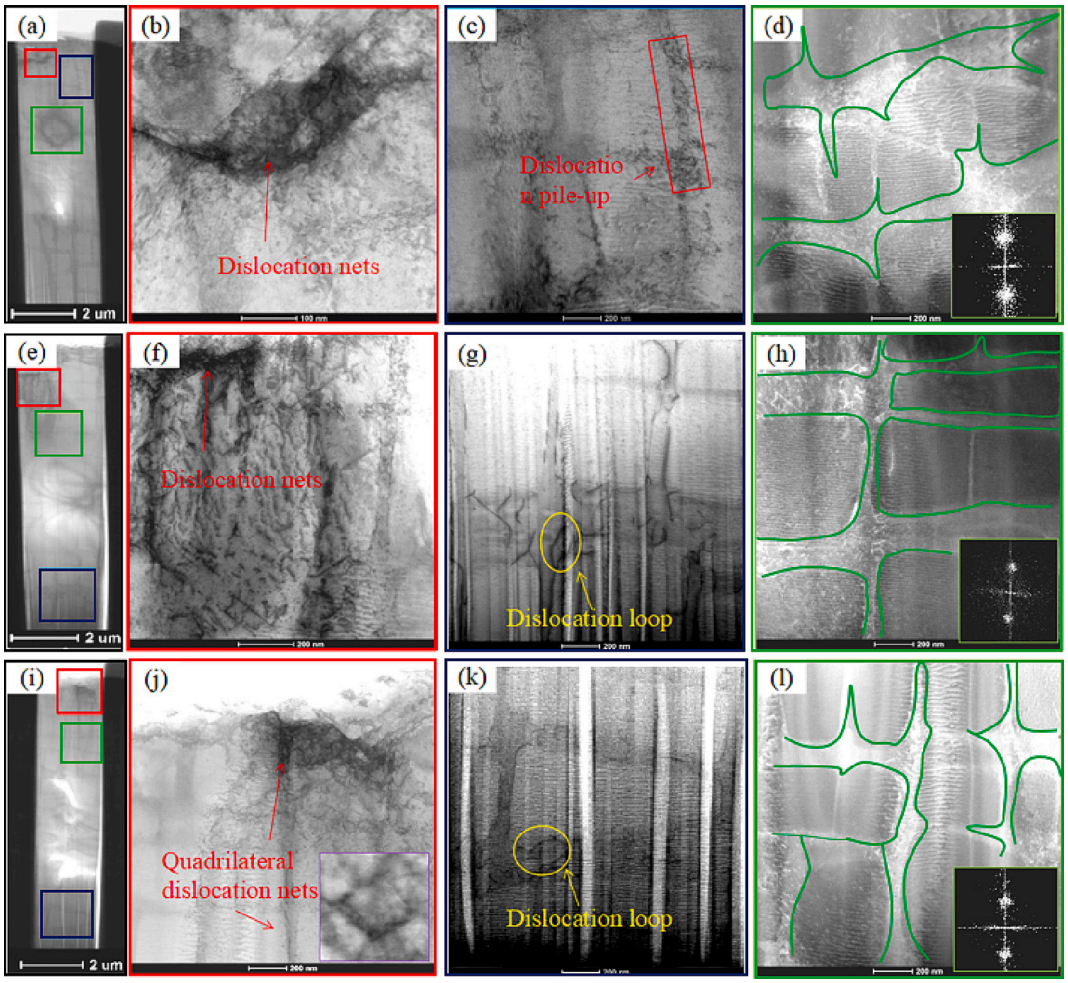

Fig. 10. Evolution of dislocations near fatigue source with different deviation angles: (a)-(d) 0°, (e)-(h) 10°, (i)-(l) 20°.

uniform, and some γ' phases can still maintain a cubic structure. When the nickel-based single crystal alloy is heat-treated, the γ' phase is completely embedded in the matrix γ phase to form a coherent interface with the γ phase, while the coherent strain and interfacial energy of the two phases are both at a lower stage. Plastic deformation occurs during the fatigue process due to the combined action of cyclic stress and high temperature. The yield strength of the γ phase is lower than that of the γ' phase, and dislocations are first generated in the γ phase. As the fatigue progresses, the reciprocating motion of dislocations in the γ phase channel causes the dissolution of the γ' phase, which will make the coherent interface gradually become a noncoherent interface, and the strengthening effect of the coherent interface will continue to weaken. With the accumulation of cyclic plastic deformation, the interface energy increases, so the activation energy required for element diffusion decreases [28]. To maintain a lower surface energy, some elements begin to dissolve into the matrix γ phase, and the cubic morphology also changes significantly.

Stripe-like structures are found in the γ' phase of the single crystal samples with different deviation angles after fatigue fracture, and the stripe directions are parallel to each other and arranged periodically, as shown in Fig. 10 (d), Fig. 10 (h), and Fig. 10 (i). The analysis shows that the streak-like structure after fatigue is a transmission moiré fringe, which is formed by the relative dislocation and superposition of the upper and lower crystal structures in the γ' phase. The moiré fringes are in the most severe region of γ' phase dissolution, which is due to the combined action of cyclic stress and high temperature in the later stage of fatigue, resulting in the dissolution of the γ' phase not only at the edges but also at the cubic phase. As fatigue progresses, the magnitude of the force exerted varies from place to place. Under the action of stress, atomic layers with different thicknesses will have local micro-dislocation, and the dislocated atomic layers will be superimposed on each other to form moiré fringes. Fig. 10 (a), 10 (e), and 10 (i) show that moiré fringes are formed close to the surface area of the sample, which further indicates that the local plastic deformation of the surface area of the sample is not uniform during the fatigue process. At deviation angles of 0°, 10°, and 20°, the dislocation densities are 4.32×10^9 cm^{-2}, 5.74×10^9 cm^{-2}, and 6.71×10^9 cm^{-2}, respectively. With the increase in dislocation density in the γ' phase, the ordered structure of γ' is disrupted, resulting in a decrease in the strength of the γ' phase. Since the γ' phase is the primary strengthening phase in nickel-based single crystal alloys, accounting for approximately 70% of the alloy composition, an increase in dislocation density leads to a reduction in fatigue life.

3.5. Evolution behavior of dislocation population at 980 °C/640 MPa

Under the stress amplitude of 640 MPa, the microstructure is shown in Fig. 11 when the deviation angle is 0°. There are only a few dislocations in the γ' phase, as shown in the position of the white arrow in Fig. 11 (c). However, a large number of dislocations exist in the matrix γ phase, as shown in the position of the blue arrow in Fig. 11 (c). The dislocation activity is confined to the matrix γ phase, indicating that dislocations first nucleate, initiate and evolve within the matrix γ phase during fatigue. With the progression of fatigue, dislocations continuously multiply in the γ phase, and the dislocation density increases accordingly, resulting in the slip motion of dislocations in the matrix γ phase. Due to the higher strength of the γ' phase compared to that of the

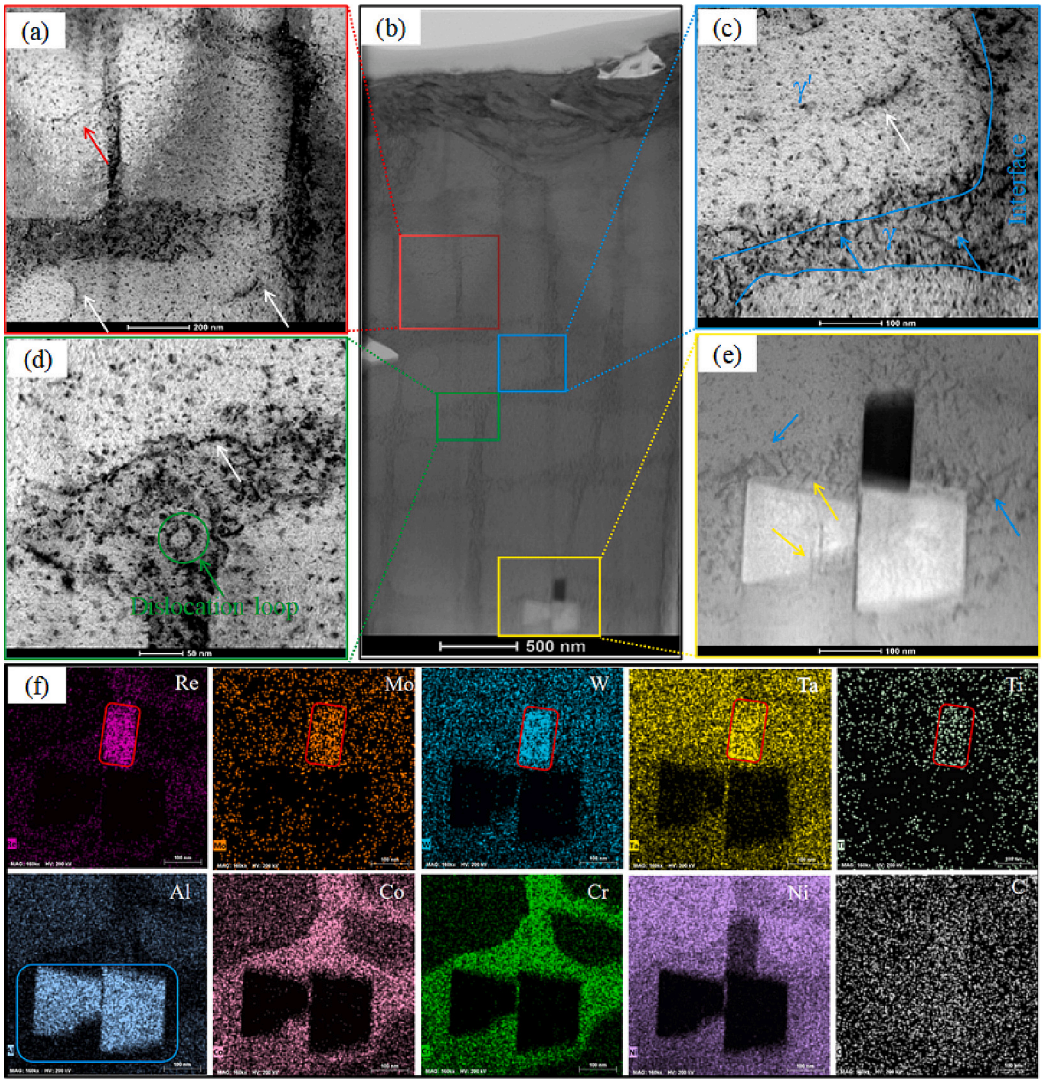

Fig. 11. Microstructural images at a high stress of 640 MPa when deviation angle is 0°: (a) magnified area image of red box in panel (b), (b) evolution of dislocations near fatigue source, (c) magnified area image of blue square in panel (b), (d) magnified area image of green square in panel (b), (e) magnified area image of yellow square in panel (b), (f) precipitate EDS surface scan image. (For interpretation of the references to colour in this figure legend, the reader is referred to the web version of this article.)

γ phase, it is difficult for dislocations to cut into the γ' phase, and the dislocation motion is hindered at the two-phase interface. With the increase in dislocations at the interface, the interaction between dislocations is enhanced, which in turn causes a large number of entanglements between dislocations. The dislocations are pinned at the interface, which increases the motion resistance of other dislocations and improves the ability to resist plastic deformation in the fatigue process. The existence of dislocation loops is found in the γ phase, as shown by the green arrow in Fig. 11 (d). The strength of the γ' phase is high in the early fatigue stage, and it is difficult for the moving dislocation to cut the γ' phase, causing the dislocation to bend and bypass the γ' phase and leaving a dislocation loop structure in the γ phase. In this case, the deformation mechanism is the Orowan mechanism in which dislocations bypass the second phase. In the later fatigue stage, the γ' phase is dissolved, and the strength decreases due to the local microregion stress concentration, leading to dislocation cutting into the γ' phase. The dislocation lines are cut from the γ phase through the phase interface to the γ' phase on both sides, as shown by the red arrows in Fig. 11 (a). When the deviation angle is 0°, the dislocations mainly move in the Orowan mechanism in the initial stage of fatigue, the dislocations in the later stage of fatigue phase move in the cutting γ' phase mechanism, and moiré fringes are not formed. Therefore, the γ' phase can maintain a high strength during the fatigue process, and the fatigue life is the longest when the deviation angle is 0°.

There are light and dark contrast precipitates inside the nickel-based single crystal alloy after fatigue fracture, as shown in Fig. 11 (e). At the same time, dislocation aggregation is observed near the precipitates, as shown by the blue arrows in Fig. 11 (e). During the fatigue process, the stress change near the precipitates causes the formation of dislocations here first, and the existence of the precipitates causes the movement of dislocations in the γ phase to be hindered and gather nearby. It can be seen from the EDS image in Fig. 11 (f) that the dark precipitate is topologically close-packedphases (TCP) phase and the bright precipitate is Al element.

Fig. 12 shows the microstructure near the fatigue source after fatigue fracture when the deviation angle is 10°. As shown in Fig. 12 (b), the dislocation distribution is not uniform, and the dislocation density decreases from top to bottom (the upper part of the image is close to the surface of the sample). During the fatigue process, the plastic deformation of the surface of the sample is larger than that of the interior, resulting in uneven dislocation density on the surface and interior.

There is a four-deformed dislocation network structure in the area close to the surface of the sample, as shown in the yellow box in Fig. 12 (c). The (−11−1) and (11−1) slip planes are activated during the fatigue process, and the interactive motion of dislocations produces a dislocation network structure. In the later stage of fatigue, the structure of the dislocation network is destroyed with the increase in dislocation density at the interface, which leads to the loss of coherence effect at the two-phase interface. A large number of dislocations are cut into the γ' phase due to the local microdomain stress concentration caused by the

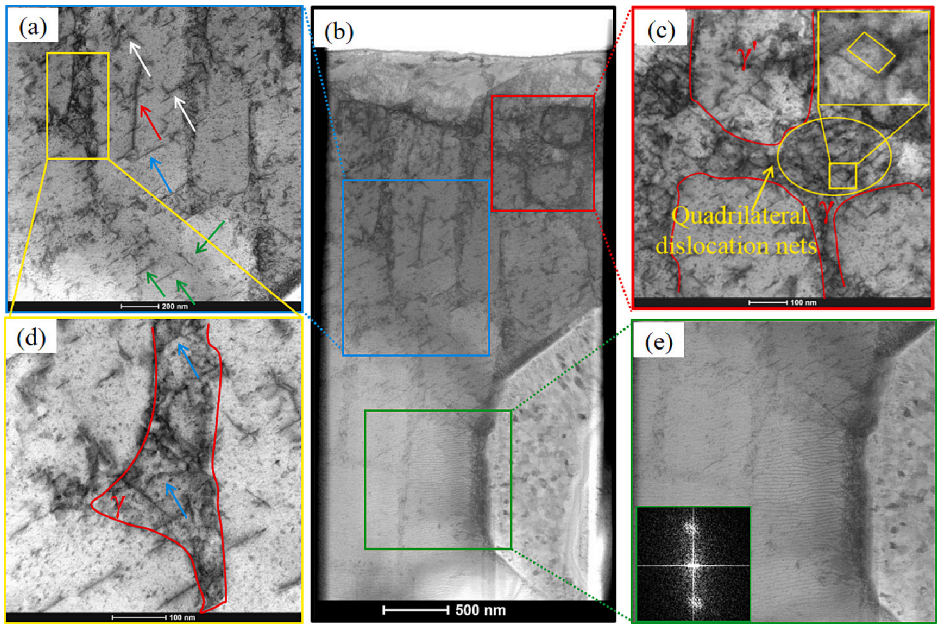

Fig. 12. Microstructure images at a high stress of 640 MPa when deviation angle is 10°: (a) magnified area image of blue box in panel (b), (b) evolution of dislocations near fatigue source, (c) magnified area image of red box in panel (b), (d) magnified area image of yellow box in panel (a), (e) magnified area image of green box in panel (b). (For interpretation of the references to colour in this figure legend, the reader is referred to the web version of this article.)

accumulation of dislocations. This reduces the degree of ordering within the γ' phase, which further reduces the strength of the γ' phase, resulting in a reduction in fatigue life, as shown by the green, white and red arrows in Fig. 12 (a). At the same time, the deflection of dislocation lines in the γ' phase is observed, which indicates that the dislocations slip on different slip planes, as shown by the white arrows in Fig. 12 (a). The cross-slip motion along the (11–1) slip plane is shown by the blue arrows in Fig. 12 (a). When the deviation angle is 10°, there are also dislocation lines along the (01−1) slip plane, as shown by the red arrow in Fig. 12 (c).

Therefore, when the deviation angle is 10°, the main mechanism of dislocation motion is that a single dislocation cuts the γ' phase, which destroys the ordered structure of the γ' phase, resulting in a decrease in its strength and fatigue life. At the same time, the streak structure is found in the fatigue process. The analysis found that this is due to the plastic deformation of the γ' phase in the microdomain caused by the combined action of cyclic stress and high temperature in the later stage of fatigue, and the atoms are superimposed on each other to form transmission moiré fringes. When the deviation angle is 20°, as with the deviation angle of 10°, the uneven plastic deformation during the fatigue process leads to the uneven distribution of dislocations, and the closer to the surface of the sample, the greater the dislocation density is. Meanwhile, there is the dislocation network structure shown in Fig. 13 (a), which is different from the quadrilateral dislocation network structure when the deviation is 10°. The dislocation network structure is formed by the movement of movable dislocations in the matrix channel to the γ/γ' interface, where screw dislocations on different slip planes meet and react with each other. When a dislocation network is formed, the lattice mismatch stress of the two-phase interface will be relaxed, which can reduce the stress concentration and the interface energy of the two phases, and stabilize the interface structure. The streak structure is found in the fatigue process. The analysis found that this is due to the plastic deformation of the γ' phase in the microdomain caused by the combined action of cyclic stress and high temperature in the later stage of fatigue, and the atoms are superimposed on each other to form transmission moiré fringes, as shown in the purple square area in Fig. 13 (a). As the fatigue progresses, the interfacial dislocation plugging produces stress concentration, which provides kinetic energy for the movement of dislocations and destroys the interfacial dislocation mesh structure. When the dislocation network is destroyed, the γ' phase is cut in the form of dislocation pairs to form the superdislocation structure shown by the blue arrow in Fig. 13 (c). Meanwhile, the single dislocation cuts the γ' phase, as shown by the white arrows in Fig. 13 (d), the ordered structure of the γ' phase is destroyed, and the intensity of the γ' phase is reduced. At the same time, some dislocation lines in the matrix γ phase are characterized by nearly right-angle kinks, as shown by the red arrows in Fig. 13 (c), as well as the cross-slip motion of the dislocation along the (−11–1) slip plane, as shown by the green arrow in Fig. 13 (d).

After fatigue fracture, black precipitates are observed inside the nickel-based single crystal alloy in scanning transmission electron microscope-bright field (STEM-BF) mode, and the size of the precipitates is approximately 100 × 150 nm, as shown in Fig. 13 (e). Clustering of dislocations near the precipitates is observed, as indicated by the yellow arrows in Fig. 13 (e). The changes of stress near the precipitates during the fatigue process lead to the formation of dislocations here first, and then the dislocations are enriched around them. It can be seen from the EDS surface scanning results that the black precipitates are enriched in elements such as Cr, Re, and Mo and are mainly σ phase-type TCP phases. When the deviation angle is 20°, the paired dislocation shear γ' phase is the main failure mode. When a lattice vector in the γ phase is a/2 ⟨110⟩ and the total dislocation slips into the γ' phase, the ordered structure of the γ' phase itself will be destroyed, and an antiphase boundary (APB) will be formed. When another a/2 < 110> full dislocation also enters the γ' phase, the γ' phase will be restored to the corresponding ordered structure. Therefore, the paired dislocations in the γ' phase in nickel-based single crystal alloys form superdislocations.

Fig. 14 (a) is a TEM image of dislocations in the γ' phase, and Fig. 14 (b) is a high-resolution atomic image of a pair of superdislocations in Fig. 14 (a). The two dislocation lines (white dashed lines) are parallel to each other, and the distance between them is approximately 26 nm, which is the width of the antiphase domain boundary. It is found that two partial dislocations have the same core structure, and both appear to be inserted into one layer of (1–11) half-atom planes as shown in Fig. 14 (d) and 14 (e). Stacking faults can be generated when a layer of closely packed {111} semiautomatic planes is inserted or extracted from the face-centered cubic crystal structure. The junction between the perfect

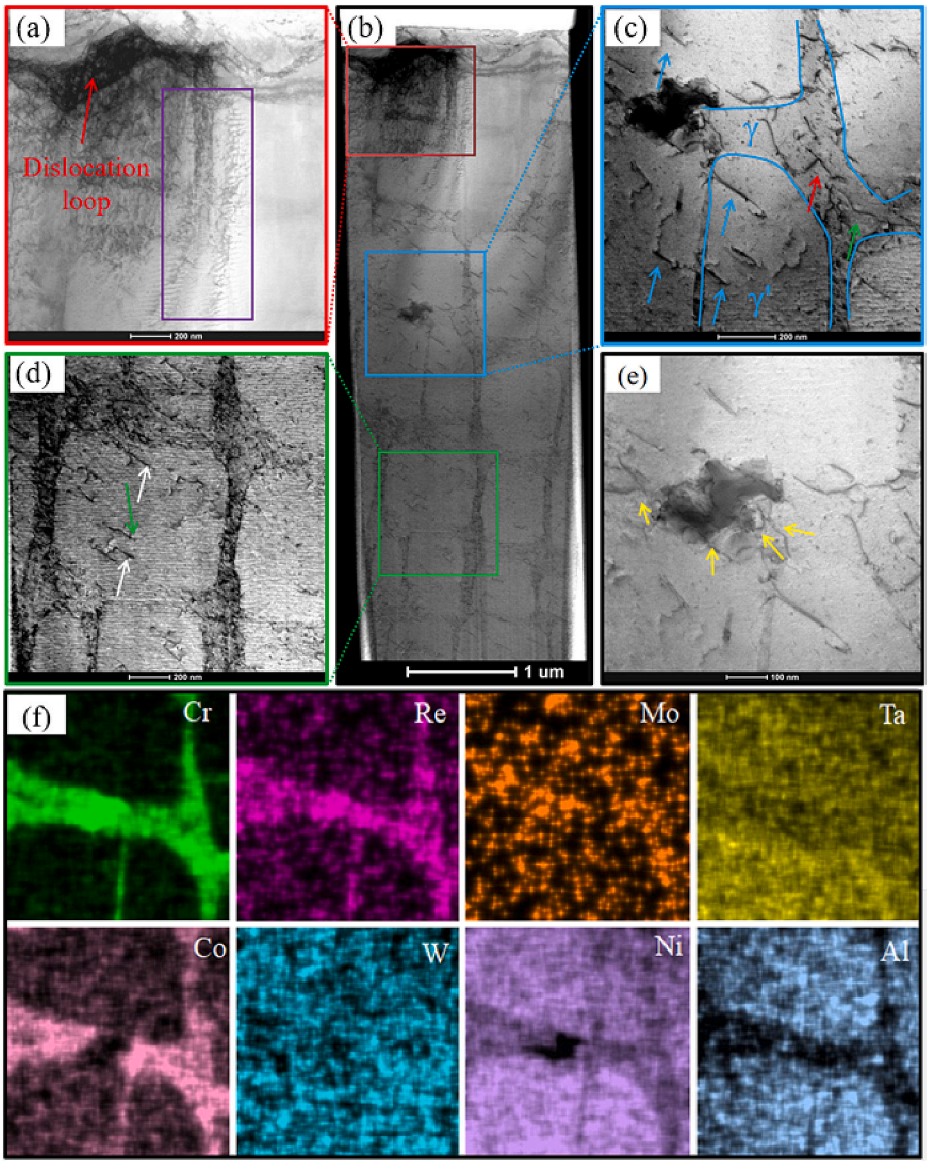

Fig. 13. Microstructure images at a high stress of 640 MPa with a deviation angle of 20°, (a) magnified area image of red box in panel (b), (b) evolution of dislocations near fatigue source, (c) magnified area image of blue box in panel (b), (d) magnified area image of green box in panel (b), (e) magnified image of precipitated phase region, (f) EDS surface scan image of precipitate in (e). (For interpretation of the references to colour in this figure legend, the reader is referred to the web version of this article.)

lattice and the stacking fault is a frank dislocation, and the burger vector $b = a/3\ \langle 1{-}11\rangle$ of the incomplete Frank dislocationis an edge dislocation.

Fig. 14 (f) is obtained by enlarging the intersection of the right side of a frank incomplete dislocation and the perfect lattice in Fig. 14 (b). Fig. 14 (f) shows that the distribution of atoms on both sides of the white dislocation line is not on the same line, and there is an obvious deflection phenomenon, which is caused by the slip motion of the lattice on both sides of the dislocation line on the (1–11) plane. This type is the lattice slip induced by the Shockley dislocation. From the atomic structure of the core region of the incomplete dislocation Shockley, it can be seen that there is no semiatomic plane, and the projection line of the (1–11) plane is formed by an inclined straight line. It becomes a broken line, which is caused by the incomplete slip of the (1–11) atomic layer and its Burger vector $b = a/6$ [1–21]. The super dislocation in the γ' phase is decomposed into two super component dislocations, and the corresponding super component dislocations are decomposed into frank and shockley incomplete dislocations. Then, a dislocation lock configuration will be formed. According to the Thompson notation [29], the dislocation decomposition process is:

$$\begin{cases} 2BD = BA + BA \\ a[01\bar{1}] \end{cases} \rightarrow \frac{\partial}{2}[01\bar{1}] + \frac{\partial}{2}[01\bar{1}]2BD$$

$$= \partial A + \partial B\frac{a}{2}[01\bar{1}] \rightarrow \frac{\partial}{3}[01\bar{1}] + \frac{\partial}{6}[\bar{2}1\bar{1}] \quad (1)$$

The slip plane of the shockley incomplete dislocation is (11–1), the dislocation line direction is [2–11], and it is a mixed dislocation. The Burger vector of Frank incomplete dislocation is perpendicular to plane (1–11), the half atomic plane is the (1−1−1) plane located at (011), and the dislocation line is perpendicular to the Burger vector, which is an edge type dislocation. In Frank's incomplete dislocation, the Burger vector is on any {111} plane, and it is a dislocation that will not slide and move under the action of an external force. In shockley incomplete

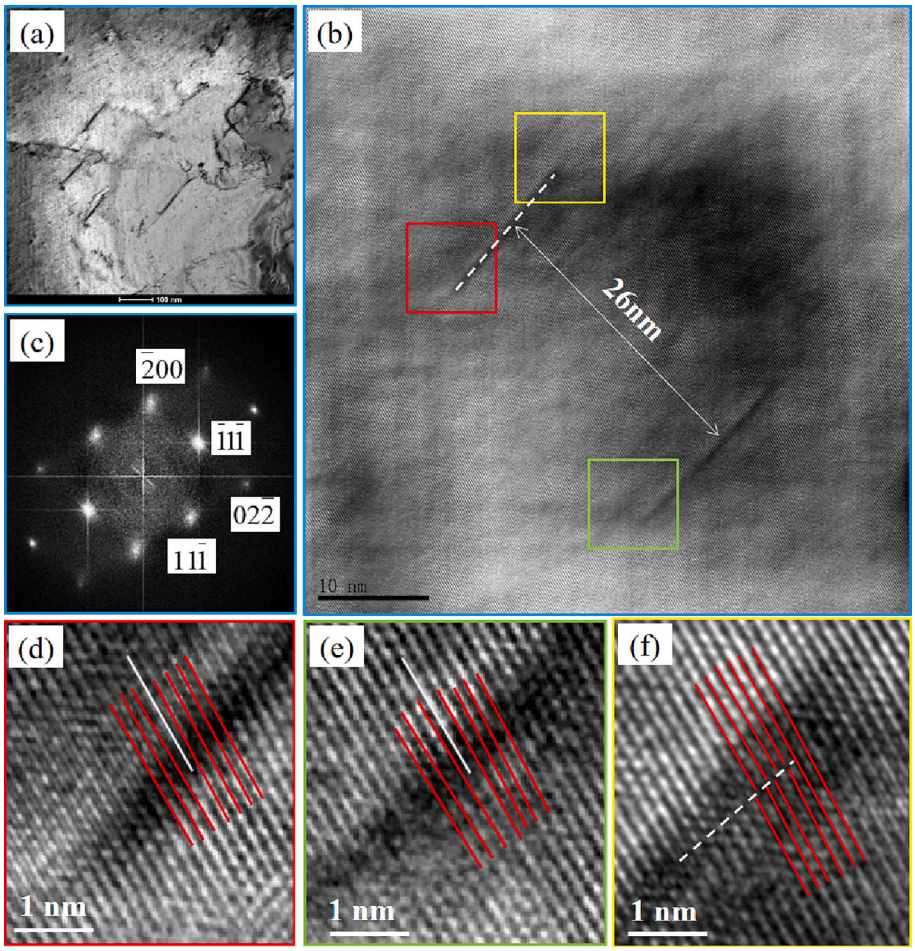

Fig. 14. (a) TEM image of superminute dislocations with an off-angle of 20°, (b) high-resolution atomic image of superfractionated dislocations, (c) electron selected area diffraction pattern with incident direction of electron beam as [011], (d) magnified frank incomplete dislocation core structure of red area in (b), (e) core structure of frank's incomplete dislocation after magnification of green area in (b), (f) shockley incomplete dislocation core structure after magnification of yellow area in (b). (For interpretation of the references to colour in this figure legend, the reader is referred to the web version of this article.)

dislocations, they can only perform slip motion and cannot perform climbing motion [30,31]. When the distance between the two incomplete dislocations increases, their stacking fault energy also increases. This will hinder the sliding of the shockley incomplete dislocation so that the full dislocation in the γ' phase will be locked. The type of dislocation configuration is called "dislocation locking." The diffusion can only take place when the higher energy is supplied, thus resulting in a higher fatigue life at the 20° deviation than at the 10° deviation.

4. Conclusions

The fatigue life of nickel-based single-crystal alloys decreases with increasing stress amplitude, and the dislocation motion mechanisms under different stress amplitudes are different. At 980 °C/600 MPa, the fatigue life decreases with increasing deviation from the [001] orientation angle, from 1.678×10^6 cycles to 2.81×10^5 cycles. The fatigue source starts from the subsurface shrinkage cavity of the sample, which initiates crystallographic cracks. When the deviation angle is 0°, the dislocations are mainly climbing motion. When the deviation angle is 10° and 20°, the Orowan motion mechanism bypasses the second phase. At deviation angles of 0°, 10°, and 20°, the dislocation densities are 4.32×10^9 cm^{-2}, 5.74×10^9 cm^{-2}, and 6.71×10^9 cm^{-2}, respectively. The increase in dislocation density leads to a reduction in fatigue life, and the fatigue mode is crystallographic fracture. At 640 MPa/980 °C, the fatigue life is 7.82×10^5 cycles when the deviation angle is 0°, 2.16×10^5 cycles when the deviation angle is 10°, and 2.53×10^5 cycles when the deviation angle is 20°. When the deviation angle is 0° and 20°, it is the crystal fracture mode. When the deviation angle is 10°, it is an amorphous fracture mode. When the deviation angle is 0°, the Orowan deformation mechanism is mainly in the early stage of fatigue, while in the later stage of fatigue, a small number of dislocations cut the γ' phase. When the deviation angle is 10°, the single dislocation mainly shears the γ' phase. When the deviation angle is 20°, the paired dislocation shearing γ' phase is the dominant failure mechanism.

CRediT authorship contribution statement

Zhuangzhuang Mao: Conceptualization, Writing – review & editing, Methodology, Validation, Data curation, Formal analysis. **Yingbin Zhu:** Methodology, Validation, Data curation, Formal analysis, Writing – review & editing. **Yao Zhao:** Data curation, Formal analysis, Methodology, Validation. **Huimin Xie:** Funding acquisition, Conceptualization, Methodology. **Yanhong Yang:** Data curation, Formal analysis, Methodology. **Xianfu Huang:** Formal analysis, Methodology, Conceptualization, Data curation. **Zhanwei Liu:** Funding acquisition, Conceptualization, Methodology, Resources, Supervision, Validation, Writing – review & editing.

Declaration of Competing Interest

The authors declare that they have no known competing financial interests or personal relationships that could have appeared to influence the work reported in this paper.

Data availability

Data will be made available on request.

Acknowledgments

This work was financially supported by the National Science and Technology Major Project (2017-VI-0003-0073), the National Natural Science Foundation of China (11972084), the National Key Research and Development Program of China (Grant No.2017YFB1103900), the Beijing Natural Science Foundation (1192014), and the BIT Research and Innovation Promoting Project (Grant No. 2022YCXY012).

References

[1] W.C. Yang, C. Liu, P.F. Qu, K.L. Cao, J.R. Qin, H.J. Su, J. Zhang, L. Liu, Strengthening enhanced by Ru partitioned to γ' phases in advanced nickel-based single crystal superalloys, Mater. Charact. 186 (2022), 111809.
[2] Z.P. Zhang, J.D. Liu, K.Q. Qiu, Y.Y. Huang, J.G. Li, X.G. Wang, J.L. Liu, M. Wang, M.K. Zou, Y.Z. Zhou, Effects of brazing temperature on microstructure and high-temperature strength of joints using a novel fourth-generation nickel-based single crystal superalloy, Met. Mater. Int. 29 (2) (2023) 444–456.
[3] Y. Du, Z. Tan, Y.H. Yang, X.G. Wang, Y.Z. Zhou, J.G. Li, X.F. Sun, Creep properties of a nickel-based single crystal superalloy with low density, Met. Mater. Int. (2021) 1–6.
[4] J. Lan, W.D. Xuan, Y. Han, Y.S. Li, H.Z. Wu, W. Shao, C.J. Li, J. Wang, Z.M. Ren, Enhanced high temperature elongation of nickel based single crystal superalloys by hot isostatic pressing, J. Alloy. Compd. 805 (2019) 78–83.
[5] Z.Y. Song, Influence of load interaction between creep and TMF on the life of single crystal nickel-based superalloy, Mater. Sci. Forum 1027 (2021) 99–106.
[6] G.Y. Wang, S. Zhang, S.G. Tian, N. Tian, G.Q. Zhao, H.J. Yan, Microstructure evolution and deformation mechanism of a [111]-oriented nickel-based single-crystal superalloy during high-temperature creep, J. Mate. Res. Technol. 16 (2022) 495–504.
[7] W.S. Xia, X.B. Zhao, Q.Z. Yue, W.D. Xuan, Q.H. Pan, J.W. Wang, Q.Q. Ding, H. B. Bei, Z. Zhang, Competitive deformation induced by TCP precipitation and creep inconsistency on dendritic structures in a nickel-based single crystal superalloy crept at high temperatures, Mater. Charact. 187 (2022), 111855.
[8] N. Tian, G.Q. Zhao, T. Meng, S.G. Tian, L.R. Liu, H.J. Yan, G.Y. Wang, F.W. Jin, Ultra-high-temperature creep behavior of a single-crystal nickel-based superalloy containing 6% re/5% Ru, Mater. Charact. 180 (2021), 111394.
[9] Y.C. Zhao, H.S. Gao, Z.X. Wen, X.H. Zhang, Y.Q. Yang, Z.F. Yue, Combined elastic-plastic energy driving criteria of rafting behavior for nickel-based single crystal superalloys, Mat. Sci. Eng. A. 758 (2019) 154–162.
[10] X.F. Yu, S.G. Tian, M.G. Wang, S. Zhang, X.D. Lu, S.S. Cui, Creep behaviors and effect factors of single crystal nickel-base superalloys, Mat. Sci. Eng. A. 499 (1–2) (2009) 352–359.
[11] D. Holländer, D. Kulawinski, A. Weidner, M. Thiele, H. Biermann, U. Gampe, Small-scale specimen testing for fatigue life assessment of service-exposed industrial gas turbine blades, Int. J. Fatigue 92 (2016) 262–271.
[12] W. Maktouf, K. Ammar, I. Ben Naceur, K. Saï, Multiaxial high-cycle fatigue criteria and life prediction: application to gas turbine blade, Int. J. Fatigue 92 (2016) 25–35.
[13] W.W. Zhang, X.G. Liu, M.Y. Zhu, Y. Guo, H.Y. Qin, Q. Tian, Precipitation characteristics of γ'precipitates of the GH4742 nickel-based superalloy at a slow cooling rate, J. Alloy. Compd. 941 (2023), 169013.
[14] L. Liu, J. Meng, J.L. Liu, T. Jin, X.D. Sun, H.F. Zhang, Effects of crystal orientations on the cyclic deformation behavior in the low cycle fatigue of a single crystal nickel-base superalloy, Mater. Des. 131 (2017) 441–449.
[15] L. Liu, J. Meng, J.L. Liu, H.F. Zhang, X.D. Sun, Y.Z. Zhou, Effects of crystal orientations on the low-cycle fatigue of a single-crystal nickel-based superalloy at 980° C, Acta. Metall. Sin-Engl. 32 (2019) 381–390.
[16] J.L. Zhou, W.J. Gao, L.E. Liu, T. Yi, W.X. Jiang, J. Wang, Y.F. Zhang, Z. Zhang, In-situ SEM study on fatigue crack behavior of a nickel-based single crystal alloy at 950° C and 1050°C, Mater. Charact. 199 (2023), 112763.
[17] J.S. He, X.L. Wang, H.J. Zhou, X.T. Wang, Low cycle fatigue of a γ'-strengthened co-based single crystal superalloy at 900° C, Mater. Charact. 185 (2022), 111720.
[18] X.Z. Dou, L.W. Jiang, J.X. Song, D.G. Wang, Exploring low cycle fatigue anisotropy and the failure mechanism of the DD412 single crystal alloy for aeroengines, Int. J. Fatigue 169 (2023), 107487.
[19] Q. Yin, Y.D. Lian, Z.X. Wen, H.Q. Pei, J.D. Wang, Z.F. Yue, Atomic simulation of the effect of orientation on tensile/compressive properties in nickel-based single crystal superalloys, J. Alloy. Compd. 893 (2022), 162210.
[20] S.N. Gu, H.S. Gao, Z.X. Wen, H.Q. Pei, Z.W. Li, Y.C. Zhao, Z.F. Yue, Creep characteristics of directionally solidified turbine blades based on the difference in original casting characteristics, J. Alloy. Compd. 884 (2021), 161055.
[21] C.M.F. Rae, R.C. Reed, Primary creep in single crystal superalloys: origins, mechanisms and effects, Acta Mater. 55 (3) (2007) 1067–1081.
[22] G.R. Leverant, B.H. Kear, The mechanism of creep in gamma prime precipitation-hardened nickel-base alloys at intermediate temperatures, Metall. Mater. Trans. B Process Metall. Mater. Process. Sci. 1 (1970) 491–498.
[23] B. Zhang, R. Q. Wang, D. Y. Hu, K. H, Jiang, J. X. Mao, F. L. Jing, X. Y. Hao, Stress-controlled LCF experiments and ratcheting behaviour simulation of a nickel-based single crystal superalloy with [001] orientation, Chinese. J. Aeronau. 34.8 (2021): 112–121.
[24] Z.D. Fan, J. Li, D. Wang, L.H. Lou, J. Zhang, Orientation dependence of low cycle fatigue properties of a Ni-based single crystal superalloy DD10, Rare. Metal. Mat. Eng. 47 (1) (2018) 1–6.
[25] J.J. Wang, Z.X. Wen, X.H. Zhang, Y.C. Zhao, Z.F. Yue, Effect mechanism and equivalent model of surface roughness on fatigue behavior of nickel-based single crystal superalloy, Int. J. Fatigue 125 (2019) 101–111.
[26] F. Li, Z.X. Wen, Z.Y. Wu, H.Q. Pei, Z.F. Yue, Fatigue life assessment of nickel-based single crystals considering equivalent initial flaw size model and anisotropy, Int. J. Fatigue 160 (2022), 106886.
[27] C.K. Sudbrack, D.L. Beckett, R.A. MacKay, Effect of surface preparation on the 815° C oxidation of single-crystal nickel-based superalloys, Jom. 67 (2015) 2589–2598.
[28] Y. Liu, L. Wang, J. Yu, Dissolution of γ' phase in a single crystal superalloy after high-cycle fatigue, Rare. Metal. Mat. Eng. 49 (9) (2020) 2925–2929.
[29] M. Condat, B. Décamps, Shearing of γ' precipitates by single a/2<110> matrix dislocations in a γ/γ' Ni-based superalloy, Scr. Metall. 21 (5) (1987) 607–612.
[30] R.J. Gaboriaud, J. Grilhé, On the energy of the hexagonal frank loop in face centred cubic metals, Phys. Status. Solidi-R. 51 (2) (1972) 579–587.
[31] D. Rodney, Molecular dynamics simulation of screw dislocations interacting with interstitial frank loops in a model FCC crystal, Acta Mater. 52 (3) (2004) 607–614.